Energy Storage Materials 9 (2017) 119–125

Contents lists available at ScienceDirect

Energy Storage Materials

journal homepage: www.elsevier.com/locate/ensm

Self-standing electrodes with core-shell structures for high-performance supercapacitors

Guanjie He[a], Min Ling[a], Xiaoyu Han[a], Dina Ibrahim Abou El Amaiem[b], Yuanlong Shao[c], Yaomin Li[a], Wenyao Li[d], Shan Ji[b], Bo Li[d], Yao Lu[a], Rujia Zou[d], Feng Ryan Wang[b], Dan J.L. Brett[b], Zheng Xiao Guo[a], Chris Blackman[a], Ivan P. Parkin[a,*]

[a] *Christopher Ingold Laboratory, Department of Chemistry, University College London, 20 Gordon Street, London WC1H 0AJ, U.K.*
[b] *Electrochemical Innovation Lab, Department of Chemical Engineering, University College London, London WC1E 7JE, U.K.*
[c] *Cambridge Graphene Center, Department of Engineering, University of Cambridge, 9 JJ Thomson Avenue, Cambridge CB3 0FA, U.K.*
[d] *State Key Laboratory for Modification of Chemical Fibers and Polymer Materials, College of Materials Science and Engineering, Donghua University, Shanghai 201620, China*

ARTICLE INFO

Keywords:
Tungsten nitride
Supercapacitor
Aerosol-assisted chemical vapour deposition
Density Functional Theory
In-situ transmission electron microscope

ABSTRACT

Fabrication of supercapacitor devices with the carbon cloth supported W_2N@carbon ultrathin layer core-shell structures (W_2N@C CS/carbon cloth) were realized by aerosol-assisted chemical vapour deposition (AACVD) followed by an ammonia annealing process. The representative electrodes delivered excellent areal specific capacitance of 693.0 mF cm^{-2} at 5 mV s^{-1} in a three electrode testing system, good rate capability of ~ 78% retention when the scan rate increased 10 times and superior cycling stability with ~ 91% capacitance retention after 20,000 cycles. The self-standing electrodes were manufactured for flexible asymmetric supercapacitors and assembled into coin cells with ionic electrolyte for high working voltage applications. The primary origins for the outperformance of W_2N over WO_{3-x} in acid aqueous electrolytes are uncovered by electrochemical analysis, simulation work and *in-situ* transmission electron microscope (TEM). This discovery paved the way of exploring and designing advanced metal nitride electrode materials for supercapacitors.

1. Introduction

As promising energy storage devices, supercapacitors, in particular pseudocapacitors, can provide higher power densities than most of the batteries [1]. The practical applications of commonly reported pseudocapacitor electrodes, such as an amorphous structure based on RuO_2 [2,3], MnO_2 [4] and WO_3 [5], *etc.*, call for improvement on specific capacitance and energy density. Metal nitride, is a type of electrode materials that presents excellent electrical conductivity (4000–55500 S cm^{-1}) and will improve energy storage properties. Fan et al. fabricated asymmetric supercapacitors based on TiN cathodes and Fe_2N anodes, leading to high rate and achieving stable energy storage devices [6]. They identified structural design modifications to solve the oxidation problem of metal nitrides, by methods such as carbon coating. Among all the reported metal oxides/nitrides materials in energy storage applications, tungsten-based electrodes have a series of inherent advantages, such as relatively low toxicity and cost, high theoretical specific capacitance and high stability [5,7,8]. There have been intensive studies focused on tungsten oxide materials to be employed as pseudocapacitive electrodes: MoO_{3-x}/WO_{3-x} core-shell nanowires [8]; nanoflower-like WO_3 on titanium foams [9] and WO_3/graphene composite aerogels [10]. These materials show improved electrochemical performances over pure WO_3 materials mainly through the nanostructure design. However, they still need further improvements, in fabrication techniques and performance amelioration to meet practical requirements. It is worth mentioning that there are few works that relate to tungsten nitride materials for energy storage applications [11] and no report has so far uncovered the origin of its high pseudocapacitive performance. In addition, no comprehensive research has been reported for the fabrication of devices based on tungsten nitride materials.

The methods for manufacturing self-standing electrodes involve integration of the active electrode materials and current collectors, such as elastic carbon films [12] and various metal substrates that support metal oxide materials [9,13], which avoids the complicated electrodes fabrication procedure for powdery materials. Compared with the most commonly reported self-standing electrode materials synthesis methods, such as the hydrothermal and electrochemical deposition

* Corresponding author.
E-mail address: i.p.parkin@ucl.ac.uk (I.P. Parkin).

http://dx.doi.org/10.1016/j.ensm.2017.07.005
Received 16 June 2017; Received in revised form 10 July 2017; Accepted 11 July 2017
Available online 12 July 2017

processes, chemical vapor deposition (CVD) has been demonstrated as an optimal method for surface engineering and provides promising advantages, such as being an industrially relevant technique for film production, production of uniform coatings [14]. Typically, CVD produces stronger adhesion strength between the active materials and the substrates. Recently, we have reported the growth mechanism of WO_3 nanorod arrays on glass by aerosol-assisted chemical vapour deposition (AACVD) method [14]. This method achieves films at relatively low coating temperature compared with other types of CVD [8,15] and is a potentially important technique for industrial applications due to the consequently reduced energy consumption.

The self-standing electrodes of core-shell structures on carbon cloth reported in this study were prepared by a single step AACVD (WO_{3-x} formation and carbon coating in one step) followed by an ammonia annealing process. Vertically aligned nanorods on current collectors can significantly enhance the specific surface area and act as a matrix to support other metal oxides with low electrical conductivity, such as an amorphous structure of RuO_x nanoparticles in this work. Supercapacitors were assembled by using a solid-state electrolyte for flexible devices and organic liquids for high voltage applications. The merits of enhanced electrochemical performances of W_2N materials in aqueous acid electrolyte compared with oxide counterparts were unveiled by electrochemical performances testing, Density Functional Theory (DFT) calculations and *in-situ* transmission electron microscopy.

2. Results and discussion

The synthetic methodology for W_2N@C core-shell arrays (CSA) involves two steps, as illustrated in Fig. 1. Firstly, WO_{3-x}@C CSA nanostructures were directly grown onto substrates by using $[W(CO)_6]$ in a mixture of acetone and methanol as the precursor for both tungsten and carbon sources. The uniform coating on hard, soft and porous substrates (morphology characterization for WO_{3-x}@C CSA on copper foils, nickel foams, carbon clothes in Figure S1) indicated that AACVD is a powerful technique for the fabrication of nanostructure film on various substrates. The mixture of acetone and methanol solution was used to accelerate the formation of aerosols during the AACVD process, thus decreasing the deposition temperature, making this method more suitable for commercialization (Figure S2 for installation of AACVD system). The second step is the annealing process of the WO_{3-x}@C CS/carbon cloth in the tube furnace under a slow flow rate of ammonia gas at 600 °C for 3 hours. The heating rate was controlled at 5 °C/min for mild ion exchange chemical reactions without damaging the morphology of the nanorod arrays and the core-shell structures. With the phase change during the annealing process, the colour of the electrodes changed from blue to black.

The morphology of the carbon cloth supported W_2N@C CSA was recorded by scanning electron microscopy (SEM) and shown in Fig. 2a. The W_2N form as needle-like nanorod arrays. The uniform coating can be confirmed by the low-magnification SEM images. The detailed morphology of the W_2N@C nanorod array clusters are revealed by high-magnification SEM images in Fig. 2b. The width of the single nanorod is 20~30 nm and length is more than 1 μm. Fig. 2c shows transmission electron microscopy (TEM) image of a typical single W_2N@C nanorod. The thin carbon shell can be detected to cover the W_2N nanorod. The simultaneous WO_{3-x} synthesis and carbon shell deposition during the AACVD process can be beneficial for stabilizing the metal nitrides and to further enhance the electrical conductivity. High resolution TEM (HRTEM) image were detected to reveal the clear nanostructure and phases, which displayed the carbon layer of ~ 3 nm as shown in Fig. 2d. The labelled lattice space of ~ 0.205 nm can be indexed to the (200) crystal plane of cubic structure of tungsten nitride. Those morphologies revealed by TEM images are similar to those of WO_{3-x}@C nanorods (Figure S3a, b), indicating the ammonia annealing process had no influence on the morphology of the nanorod or the carbon shell. The blue dashed circle showed the typical amorphous carbon lattice. To further illustrate the structure of the carbon cloth supported W_2N@C CS nanorods, scanning electron microscopy-energy dispersive X-ray spectroscopy (SEM-EDS) characterization was performed to obtain elemental composition and distribution information. EDS spectra revealed the target element peaks of C, W, N in the whole of the nanostructures. Fig. 2(g-i) showed the SEM mapping images of the W_2N@C CS/carbon cloth. The dense red spots proved the high tungsten content. Nitrogen overlapped with tungsten homogeneously, demonstrating nitrogen was uniformly distributed in the crystal structures. Moreover, the carbon was present at low density, corresponding to the thin layers detected from the TEM images.

X-ray Diffraction (XRD) patterns were recorded to investigate the phase changes of the electrodes before and after the annealing process in ammonia gas. The phase of the WO_{3-x} (Figure S3c) can be indexed to $W_{18}O_{49}$ (JC-PDS No. 36–0101) and W_5O_{14} (JC-PDS No. 41–0745) while the blue color of the coating indicated the oxygen vacancy features of the tungsten oxide. After the reaction with the ammonia, it is clearly observed that pure phase of W_2N was achieved successfully and the diffraction peaks of ~ 17.1°, ~ 19.8°, ~ 28.1°, ~ 33.1° and ~ 34.6° correspond to the cubic W_2N lattice of (111), (200), (220), (311) and (222) (JC-PDS No. 25–1257) with no XRD evidence of the oxide phase in Fig. 3a. The carbon peak at ~ 12° from the carbon ultrathin shell/carbon cloth substrates can be detected from both the XRD patterns before and after the annealing process in the ammonia gas. X-ray photoelectron spectroscopy (XPS) analysis showed that the C-N bonds present from C 1 s (Fig. 3b) and N 1 s (Fig. 3d) spectra, indicating the N doping into the carbon frameworks with sp^3 and sp^2 hybridized orbitals [16]. Compared with WO_{3-x} in Figure S3d, the W 4 f spectrum of W_2N (Fig. 3c) showed different compositions, which was in accordance with the Raman spectra results (Figure S4). The spin orbital positions of the W $4f_{7/2}$ and W $4f_{5/2}$ electron for W at ~ 33.2 and ~ 35.2 eV are related to W within the b.c.c W_2N structures. The chemical shifts in the core levels of the W_2N relative to W compared with the results from the literature which correspond to a charge transfer from tungsten to nitrogen during the ammonification process [17]. The W 4 f spectrum of W_2N has some residual W-O bond as WO_{3-x}, which was caused by a surface oxygen contamination layer, which is a

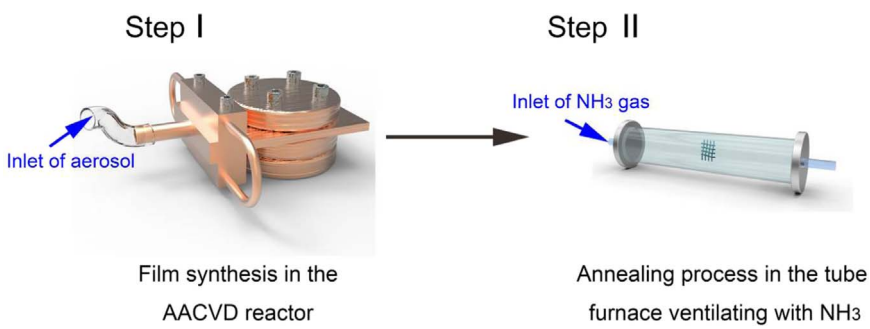

Fig. 1. Schematic illustration of the synthetic procedure of the electrodes. Two step synthesis of the carbon cloth supported W_2N@C core-shell arrays (CSA) electrodes.

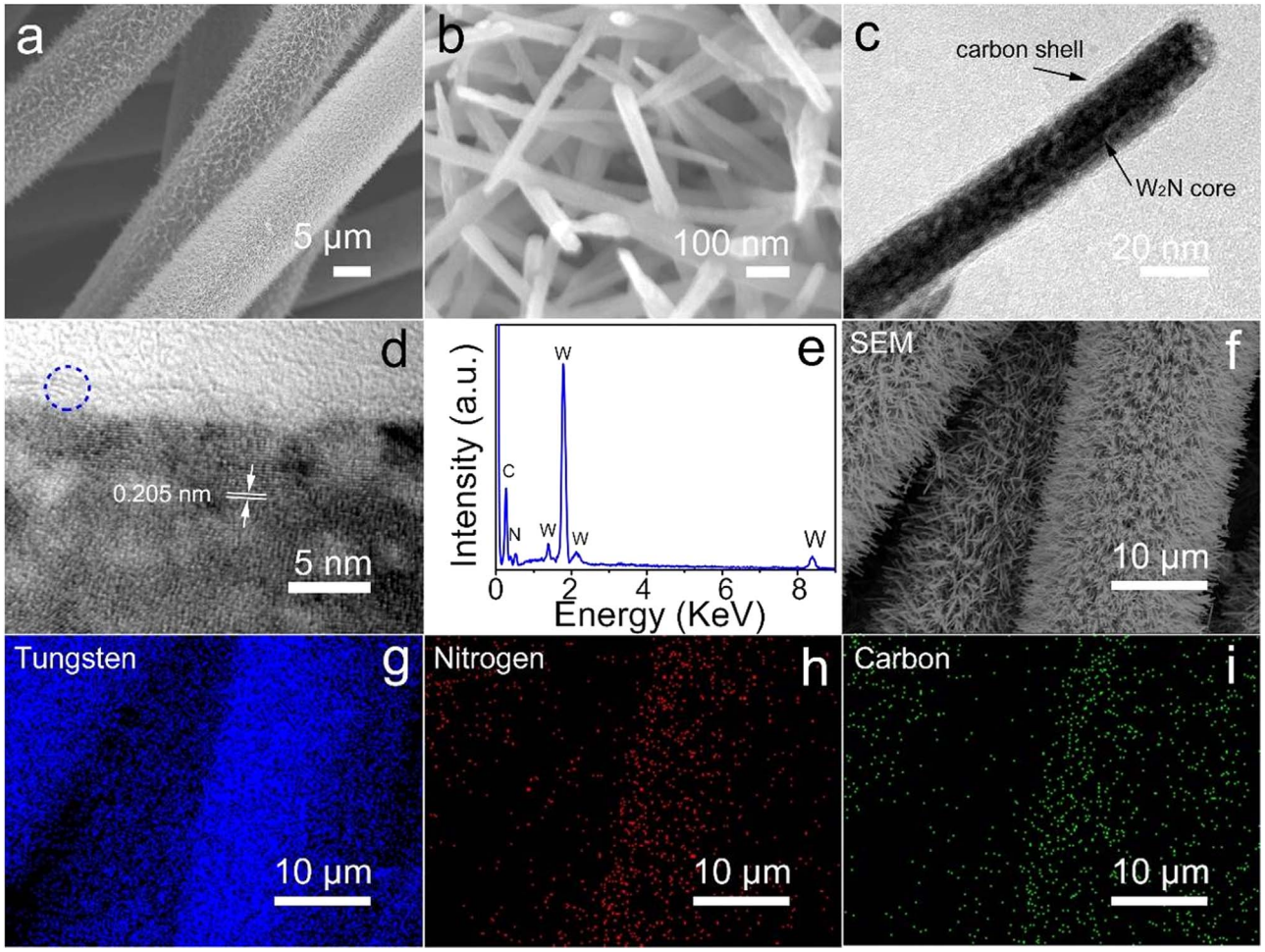

Fig. 2. Morphology characterization of the W_2N@C CS. (a), (b) Low and high magnification SEM images of the carbon cloth supported W_2N@C CS electrodes respectively; (c) TEM image of the W_2N@C CS nanorod; (d) HRTEM image of the W_2N@C CS nanorod; (e) EDS spectrum of the carbon cloth supported W_2N@C CS electrodes from SEM image; (f-i) EDS mapping images of the carbon cloth supported W_2N@C CS electrodes; f: corresponding SEM image, g: tungsten; h: nitrogen and j: carbon.

common phenomenon for metal nitride materials [17]. W-N can also be detected from N 1 s (Fig. 3d) at ~ 396 eV.

To evaluate the capacitive performance of the carbon cloth supported W_2N@C CSA, the self-standing electrodes were tested directly in three-electrode cells with 2 M H_2SO_4 solution as the electrolyte. In order to optimize the performance of the as-synthesized electrodes, different amounts of the precursor solution were used to deposit the W_2N@C CS nanorod arrays on the carbon cloth. Fig. 4a shows rate performances of the W_2N@C on carbon cloth electrodes with different volumes of precursor, calculated by the cyclic voltammetry (CV) curves (Representative CV curves in Figure S5) of at least three different samples. At a low scan rate of 5 mV s^{-1}, the areal specific capacitance increases with the mass loading of the active materials. The highest areal specific capacitance of 752.3 mF cm^{-2} can be achieved when the volume of the precursor solutions is 25 mL. However, the high loading density of the active materials blocked the porous structures (SEM of 25 mL precursor samples in Figure S6) thus curtailing the electrochemical reactions, especially at a high scan rate. Compared with other amounts of the precursor solution, 20 mL of the precursor solution gave the best performance. Compared with the morphologies of the samples from other amounts of the precusors (Figure S7), 20 mL of the precursor solution presents the most dense and uniform coating. The average areal specific capacitances of 693.0, 598.9, 519.7, 469.8, 436.2 and 410.0 mF cm^{-2} at scan rates of 5, 10, 20, 30, 40 and 50 mV s^{-1} were obtained respectively, which presented the highest specific capacitance at almost all scan rates. Considering the mass loading and gravimetric capacitance with different amount of the precursors (Figure S8), 20 mL of precursor solutions proved as the optimized volume. Hence, all the following experiments were carried out by using the optimum amount (20 mL) of precursor solution unless stated otherwise. Compared with the electrochemical performance before (WO_{3-x}@C) and after (W_2N@C) NH_3 annealing process from a galvanostatic charge-discharge (GCD) test at a current density of 3 mA cm^{-2}, W_2N@C CS realized nearly rectilinear CD curves for supercapacitor properties and longer discharge times. These results demonstrate it can possess higher specific capacitance, which is compatible with the larger enclosed area of the nitride samples from CV curves in Fig. 4c. After the annealing process, the CV curves changed from the “dolphin-like” shape to the rectangular one. The distinct pairs of the redox peaks can be detected in W_2N@C CS electrodes at 0.05 and 0.45 V for oxidation peaks and 0 and 0.39 V for reduction ones. For the WO_{3-x}@C CS electrodes, nearly undetected CV peaks are a very common feature among various tungsten oxide analogues, which is due to the tortuous ion diffusion pathway within the oxide lattice [18]. Moreover, the potential differences of the anodic and cathodic peaks can explain the reversibility of the redox reactions. The value of potential differences for W_2N@C electrodes is around 0.05 V, less than a series of reported tungsten oxide materials [5,8–10,18], suggesting the reformative reversibility of the redox reactions. Therefore, the capacitance of W_2N materials can be contributed from electrical double-layer capacitance and pseudocapacitance. The possible Faradic reactions in H_2SO_4 can be described: $W_2N + \alpha H^+ + \alpha e^- \leftrightarrow H_\alpha W_2N$. The electrical conductivity and the ion-transfer ability of the above two electrodes were further studied by EIS spectra and fitted according to the equivalent circuit model in Figure

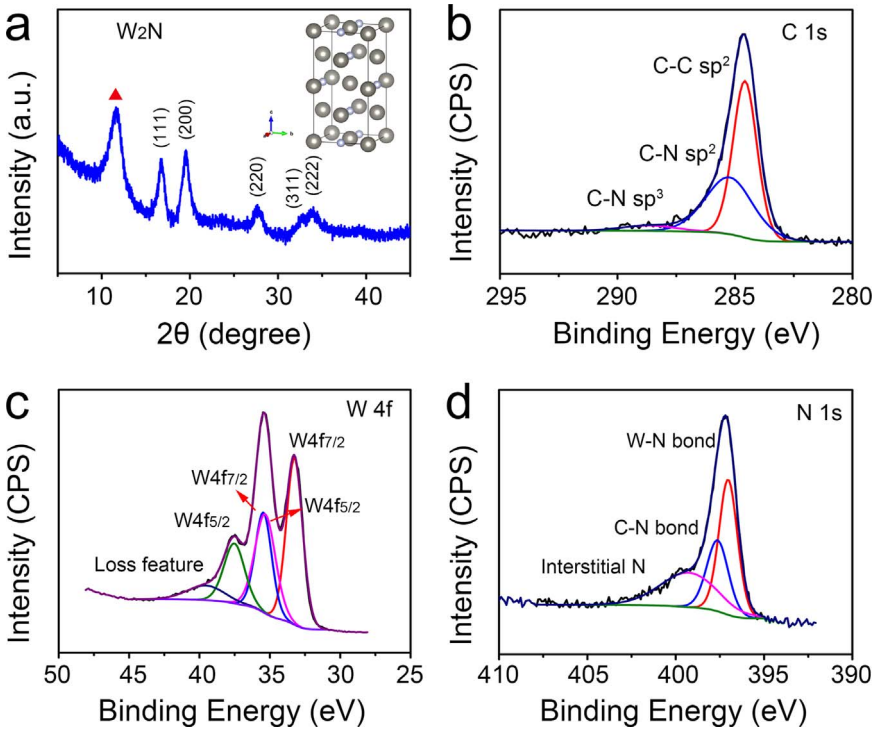

Fig. 3. Structural and Chemical analysis for the W2N@C CSA/carbon cloth. (a) X-ray Diffraction (XRD) pattern of W_2N on carbon cloth and its standard JCPDS pattern. Red triangles showing the peaks from the carbon substrate, inset in (a): crystal structures of cubic W2N, large ball: tungsten, small ball: nitrogen; X-ray photoelectron spectroscopy (XPS) spectrum of (b) C 1 s; (c) W 4 f. and (d) N 1 s.

S9a. The equivalent series resistance (R_s), containing the inherent resistances of the active materials, bulk resistance of the electrolyte and contact resistance of the interface between electrolyte and electrodes, are 0.542 and 0.588 Ω for the W_2N@C and WO_{3-x}@C electrodes, respectively. The charge transfer resistance (R_{ct}) values, reflecting the diffusion of electrons are 0.12 and 0.133 Ω for the W_2N@C and WO_{3-x}@C electrodes, respectively. The low resistance and the minor differences in resistances confirmed the carbon coating process enhances the electrical conductivity for WO_{3-x} nanorods system. For further investigation of the improved performance of the tungsten

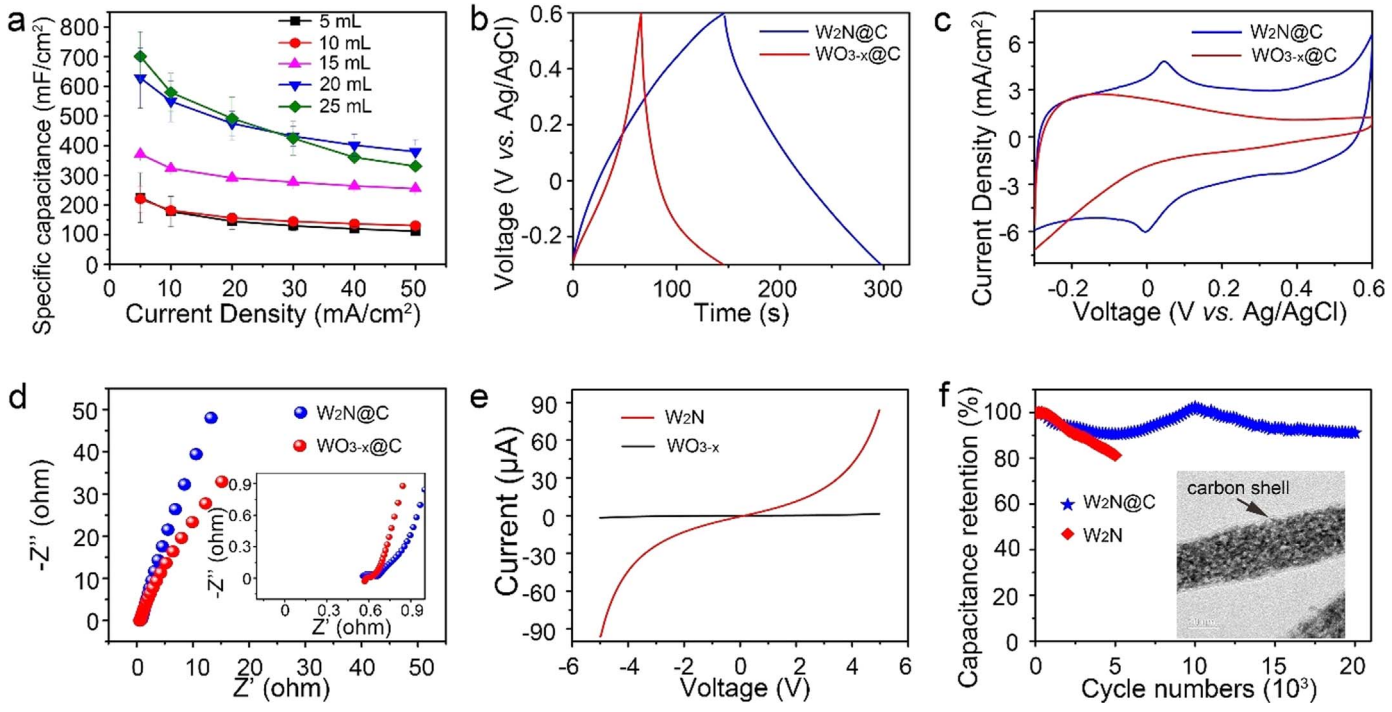

Fig. 4. Electrochemical performances evaluation of the single electrodes. (a) Rate performances of W_2N@C CSA/carbon cloth electrodes from different volumes of precursors; (b) Galvanostatic charge-discharge (GCD) curves of W_2N@C and WO_{3-x}@C on carbon cloth at 3 mA/cm^2 respectively; (c) Cyclic voltammetry (CV) curves of W_2N@C and WO_{3-x}@C on carbon cloth electrodes at 5 mV/s, respectively; (d) Electrochemical impedance spectra (EIS) of the W_2N@C and WO_{3-x}@C on carbon cloth electrodes, respectively, inset showing the high frequency range of the spectra; (e) I-V curves for the W_2N and WO_{3-x} nanorod, respectively, inset showing the TEM image of the W_2N nanorod between the probe and the tip; (f) Cycling performances of W_2N@C and W_2N on carbon cloth, the inset showing the TEM images of W_2N@C after cycling.

nitride as an electrode for supercapacitor applications compared with the oxide counterpart, the *in situ* electrical properties of the non-carbon coated W_2N and WO_{3-x} nanorod were studied by transmission electron microscopy-scanning tunneling microscopy, which was carried out within a 200 kV high resolution TEM with beam-blank irradiation at low illumination. The detailed experimental setup was shown in Figure S10, which is similar to our previous report [19]. The recorded I-V curves in Fig. 4e show a Schottky contact between the W_2N nanorod and the probe when applying a bias. The current varies from −96 to 84 μA with the voltage range from −5.0 to 5.0 V. The resistance can be calculated as 5.56×10^4 Ω (electrical conductivity of ~ 4093 S cm^{-1}); while the current changes from −1.6 to 1.4 μA at the same current range of the WO_{3-x} nanorod, which shows a resistance of 3.33×10^6 Ω (electrical conductivity of ~ 68 S cm^{-1}). These results clearly demonstrate that the electrical conductivity of the as-fabricated W_2N was ~ 2 magnitudes higher than that of the WO_{3-x} and 5–7 magnitudes higher than other commonly reported transitional metal oxide nanostructures [20,21]. The results are in accordance with the resistance comparison from the EIS spectra with WO_3/carbon cloth (Figure S9b). In order to verify the contribution of the carbon coating to the whole structures, the long-term cycling performance by repeating the CV test at a scan rate of 50 mV s^{-1} was compared between W_2N@C and W_2N on carbon clothes, respectively. As shown in Fig. 4f, a capacitance retention of 91% was seen for W_2N@C CSA/carbon cloth electrodes after 20000 cycles, which is better than that of 81.3% for W_2N/carbon cloth after 5000 cycles; the phase of the carbon shell electrodes showed almost no change, but the W_2N/carbon cloth presented the oxide phases from XRD patterns (Figure S11), this illustrates the improved cycling stability and structural stability caused by ultrathin carbon coating. The as-synthesized electrodes are among the best tungsten materials for supercapacitor application and present one of the highest specific areal capacitance values (Table S1). The inset in Fig. 4f shows the TEM images of the W_2N@C CS nanorod after cycling, in which a rougher surface topography indicates the long time of the redox reactions but kept the capping of the nanorods by the carbon shell, thus keeping the integration of the nanostructures. In order to present the successful application based on the highly conductive W_2N/carbon cloth for hierarchical nanostructures building, amorphous RuO_x nanoparticles were loaded and enhanced energy storage performance as the electrode for supercapacitors was recorded (Figure S12).

To further study the electrochemical performances of the W_2N material and its oxide counterparts as supercapacitor electrodes. The calculations of the H^* redox reaction on W_2N (200) and $W_{18}O_{49}$ (010) surfaces, which are characterized in the experiment section, were carried out based on Density Functional Theory, implanted in Vienna ab-initio Packages (VASP) [22]. Detailed comparison of different functionals and computational settings, including Projector Augmented Wave (PAW) [23] and The PBE functional [24,25] were demonstrated in the Supporting Information.

As for the WN_x binary system, in the $x < 1$ regime, there are two main phases formed: tungsten mononitride WN (hexagonal h-WN at low temperature and cubic c-WN at high temperature) and tungsten subnitride W_2N [26]. The former phases were well studied [27–31], but there are few theoretical works on the cubic W_2N [32–34]. For W_2N derived from the c-WN $Fm\bar{3}m$ structure, two possible structures are proposed, ß-W_2N and t-W_2N, shown in Fig. 5a, b. Both structures share the same positions for W, while the 50% vacancy of N happen at different sites, based on the c-WN structure. We compared the formation energies of these two structures, which defined as $E_f = E_{W_2N} - 2nE_W - nE_{N_2}$, where E_{W_2N} is the energy of ß-/t-W_2N. E_W and E_{N_2} are the chemical energies of W in bulk tungsten and N in N_2, respectively. And the n represents the numbers of N in the ß-/t-W_2N systems. As shown in Table S2, both ß- and /t-W_2N possess lower formation energy, compared with c-WN, which can conclude that both states are stable states in WN_x binary system. However, the ß-W_2N structure is more energetically favour than t-W_2N. Hence, ß-W_2N structure is selected for subsequent calculations.

For W_2N (200) and $W_{18}O_{49}$ (010) slabs (Fig. 5c and d), 2*1*1 and 1*2*1 supercells were selected for the study of H^* adsorption. A 10 Å vacuum slab added to prevent periodic interactions. The bottom half atoms were fixed, while all other atoms at the top half were fully relaxed. The k-point samplings were reduced to 15*15*1 and Gamma point only for W_2N and $W_{18}O_{49}$, respectively. The adsorption energy was calculated based on the following equation:

$$E_{ad} = E_{total} - E_{slab*} - \frac{1}{2}E_{H_2}$$

where E_{ad} is the adsorption energy. E_{total} represents the total energy of the system. E_{slab*} and E_{H2} are the energies of W_2N (200) or $W_{18}O_{49}$ (010) slabs and the chemical energy of H_2, respectively. From the top view of the W_2N (200) surfaces, there are four different possible adsorption sites, shown in Fig. 5c. To distinguish different W atoms as active sites on the surface, the W atoms with and without N atom underneath are denoted as W_1 and W_2, respectively. The T and V represent as the top and vacancy active sites for the adsorbent atom, respectively.

As shown in Table 1, the H^* tends to bond with surface tungsten in the regime of physical adsorption, Figure S13(a, b). The surface W_1 is the strongest bonding site, followed by the W_2. Both exhibit exothermic reactions. These physical adsorptions can benefit for the H^* association/dissociation reaction required in the redox reactions. Compared with N and V (Figure S13c, d), which is not H^* favoured bonding sites, the W-rich W_2N surface also provided more reaction sites. Hence, the ß-W_2N compound is not only energetically stable in structure, but also has more surface W for bonding to H^*. Moreover, as transition metals, the surface W could also be a host for multi-adsorption of H^* per site. [35] We also employed the Climbing Image Nudged Elastic Band (Ci-NEB) method to study the energy barrier of the H^* diffusion on the W_2N (200) surfaces. [36] As shown in Figure S14, the energy barriers within the surfaces is relatively large, enough to prevent further H^* diffusion. The results suggest that the H^* redox reactions occurred only at each site without additionally H^* movement of the surface.

Whereas for the $W_{18}O_{49}$ (010) surface, the relaxed structure endured a significant distortion, as shown in Figure S15, 16. Consequently, the $W_{18}O_{49}$ surface is more disordered. Meanwhile, the dangling O on the surface also provides strong bonding sites for H^*. The adsorption energy is too strong, ~ 2 eV, and results in hydrogen passivation of the $W_{18}O_{49}$ (010) surface. Detailed adsorption energy for each site (Figure S17) are listed in Table S3. The H passivation corresponds to the experimentally observed CV results in Fig. 4c. These covalent bonds are too strong for the H^* to break off reversible redox reactions, which reflected in the “dolphin-like” shape CV curve. Hence, further H passivated $W_{18}O_{49}$ (010) surface, Figure S16, will be the adsorbent for further redox reaction. However, additional H^* will not be desirable due to the relatively weak hydrogen bonds.

To evaluate the practical applications of the as-synthesized W_2N@C CSA/carbon cloth electrodes, a flexible asymmetric supercapacitor device (FASD) was assembled by using the W_2N@C CSA/carbon cloth as the negative electrode and nitrogen doped graphene on foldable commercial carbon paper (single electrode testing in Figure S18) as the positive one. Fig. 6a described the CV curves of the FASD under different voltage range from 0.8 to 1.6 V at a scan rate of 50 mV s^{-1}. It shows that the fabricated FASD functioned steadily up to an electrochemical potential window of 1.6 V (Figure S19). The shape of the CV curves deviates from the rectangular shape and the unobvious redox reaction peaks to a certain extent indicating that the asymmetric capacitance contributions were both from the pseudocapacitance and electrical double-layer capacitance (EDLC). In order to avoid side reactions, the GCD tests were performed over the voltage window of 1.2 V at current densities of 1–10 mA cm^{-2}. The excellent specific capacitance was calculated and indexed as shown in Figure S20a.

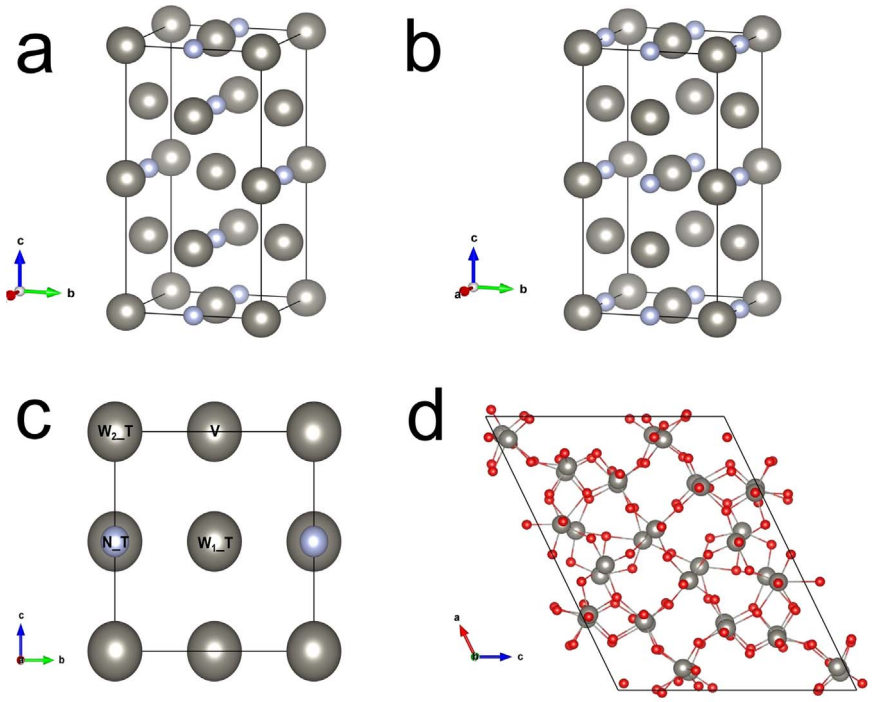

Fig. 5. Explanation of the enhanced performances of W_2N for supercapacitor electrodes by Density Functional Theory. (a) The two possible cubic structures of W_2N: ß-W_2N (a) and t-W_2N (b). The grey and light purple balls represent tungsten and nitrogen atoms, respectively. (c) The top view of W_2N (200) surface. The W atoms directly above an N atom in below are denoted as W_1, while the ones without are W_2. The T and V abbreviate for top and vacancy sites, respectively. The grey and purple balls are tungsten and nitrogen atoms, respectively. (d) The top view of $W_{18}O_{49}$ (010) surface (relaxed). The grey and purple balls are tungsten and nitrogen atoms, respectively.

Table 1.
The H^* adsorption energy (eV) at different active sites and H-W/N distance (Å) on different sites of W_2N (200) surfaces. The W_1_T, W_2_T and N_T represents the top sites on W and N, respectively. Whereas, V denoted as the N vacancy on W_2N (200) surface. W_1 and W_2 differentiated as the top W atom with or without N atom underneath.

	W_1_T	W_2_T	N_T	V
E_{ad} (eV)	−0.50	−0.06	0.17	0.39
distance (Å)	1.74	1.77	1.03	2.25

Notably a high rate capability of ~ 85.5% retention was observed when the current density was increased 10 times. The digital pictures (Figure S20b) showed that the devices can be bent at different bend angles with almost no influence on the energy storage performance (Figure S20c). The FASD delivered excellent cycling performances, with 92% capacitance retention after 5000 cycles at a current density of 10 mA cm^{-2}. The Ragone plot (inset in Figure S20d) revealed that the FASD can deliver excellent areal energy/power density. To target the high working voltage applications, symmetric devices (SD) were fabricated based on W_2N@C CSA/carbon cloth with ionic liquid as the electrolyte in coin

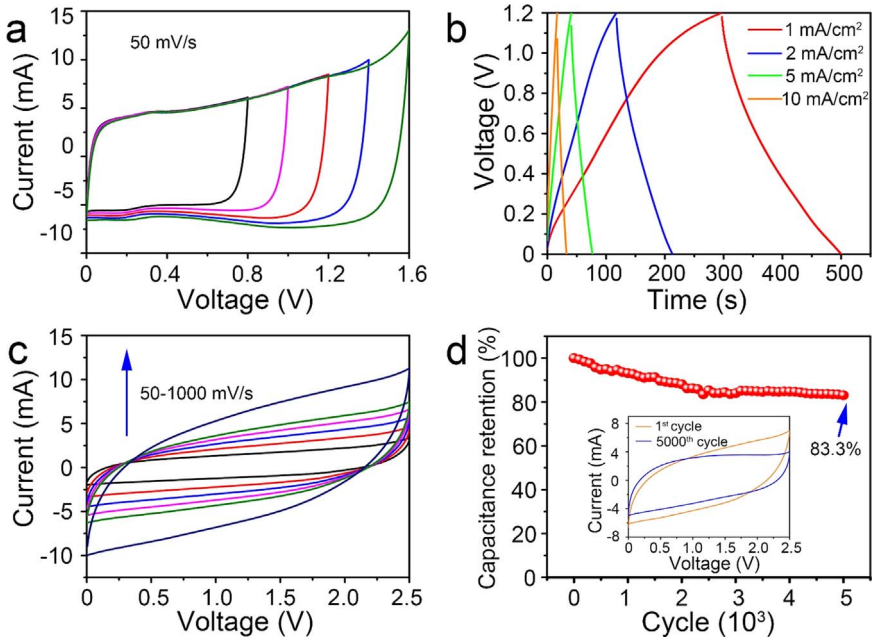

Fig. 6. Supercapacitor performance assessment. (a) CV tests of the flexible asymmetric supercapacitor device (FASD) under different voltage range; (b) GCD of the FASD at different current densities; (c) CV tests of the ionic liquid-based electrolyte for symmetric devices (SD) at different scan rates; (d) Cycling stability of the SSD at a CV scan rate of 100 mV s^{-1}.

cells and the resultant CV curves are shown in Fig. 6c. The near rectangular shape and the excellent reversibility even at the high scan rate of 1 V s^{-1} indicated high rate performance of the devices, in accordance with GCD profiles (Figure S21); the corresponding Ragone plot is shown in Figure S22a. The cycling performances were assessed by 5000 continuous CV tests at a high scan rate of 100 mV s^{-1} (Fig. 6d). The capacitance retention of 83.3% and limited discrepancy of the area for CV curves (inset in Fig. 6d) along with the Nyquist curves (Figure S22b) between the first and final cycles proved the excellent cycling stability of the ionic liquid electrolyte based SD.

In summary, we have developed an easily industrially up-scalable approach by combining AACVD and ammonia annealing process to manufacture self-standing electrodes, *i.e.* W_2N@C CSA/carbon cloth, effectively. The as-synthesized electrodes prove to be one of the highest areal specific capacitances amongst tungsten-based nanostructures with excellent rate capability and superb cycling stability, characterized using three-electrode testing. The supercapacitors have been assembled for flexible device applications and the high cell voltage use. The superiority of the tungsten nitride materials compared with the oxide counterparts for use as supercapacitor electrodes were confirmed by electrochemical analysis, theoretical calculations and *in situ* TEM. The research gives an insight for exploring the high performance of metal nitride materials as pseudocapacitor electrodes and paves the way for hierarchical nanostructure designs based on the highly conductive self-standing electrodes.

3. Experimental section

Materials synthesis and characterization parts are in Supporting information.

Acknowledgements

The authors acknowledged University College London and China Scholarship Council for the joint Ph.D. scholarship (No. 201406370157); Science and Technology Facilities Council (ST/N002385/1) for STFC/MDC Futures Early Career Award. The authors would like to thank the financial support from Engineering and Physical Sciences Research Council (EPSRC; EP/L015862/1, EP/K021192/1 and EP/N032888/1) and National Natural Science Foundation of China (Grant No. 51602193), Shanghai "Chen Guang" project (16CG63) to carry out the experiments and simulation work. The authors would also thank the use of the UCL Grace High Performance Computing Facility and associated support services, in the completion of this work.

Appendix A. Supporting information

Supplementary data associated with this article can be found in the online version at doi:10.1016/j.ensm.2017.07.005.

References

[1] V. Augustyn, P. Simon, B. Dunn, Energy Environ. Sci. 7 (2014) 1597–1614.
[2] L. Deng, J. Wang, G. Zhu, L. Kang, Z. Hao, Z. Lei, Z. Yang, Z.-H. Liu, J. Power Sources 248 (2014) 407–415.
[3] W. Sugimoto, H. Iwata, Y. Yasunaga, Y. Murakami, Y. Takasu, Angew. Chem. Int. Ed. Engl. 42 (2003) 4092–4096.
[4] H. Jiang, J. Ma, C. Li, Adv. Mater. 24 (2012) 4197–4202.
[5] Z. Chen, Y. Peng, F. Liu, Z. Le, J. Zhu, G. Shen, D. Zhang, M. Wen, S. Xiao, C.-P. Liu, Y. Lu, H. Li, Nano Lett. 15 (2015) 6802–6808.
[6] C. Zhu, P. Yang, D. Chao, X. Wang, X. Zhang, S. Chen, B.K. Tay, H. Huang, H. Zhang, W. Mai, H.J. Fan, Adv. Mater. 27 (2015) 4566–4571.
[7] V. Chakrapani, J. Thangala, M.K. Sunkara, Int. J. Hydrog. Energ. 34 (2009) 9050–9059.
[8] X. Xiao, T. Ding, L. Yuan, Y. Shen, Q. Zhong, X. Zhang, Y. Cao, B. Hu, T. Zhai, L. Gong, J. Chen, Y. Tong, J. Zhou, Z.L. Wang, Adv. Energy Mater. 2 (2012) 1328–1332.
[9] M. Qiu, P. Sun, L. Shen, K. Wang, S. Song, X. Yu, S. Tan, C. Zhao, W. Mai, J. Mater. Chem. A 4 (2016) 7266–7273.
[10] Y.-H. Wang, C.-C. Wang, W.-Y. Cheng, S.-Y. Lu, Carbon 69 (2014) 287–293.
[11] D.K. Nandi, U.K. Sen, S. Sinha, A. Dhara, S. Mitra, S.K. Sarkar, Phys. Chem. Chem. Phys. 17 (2015) 17445–17453.
[12] P. Huang, C. Lethien, S. Pinaud, K. Brousse, R. Laloo, V. Turq, M. Respaud, A. Demortiere, B. Daffos, P.L. Taberna, B. Chaudret, Y. Gogotsi, P. Simon, Science 351 (2016) 691–695.
[13] G. He, J. Li, W. Li, B. Li, N. Noor, K. Xu, J. Hu, I.P. Parkin, J. Mater. Chem. A 3 (2015) 14272–14278.
[14] M. Ling, C. Blackman, Phys. Status Solidi C 12 (2015) 869–877.
[15] S. Vallejos, P. Umek, T. Stoycheva, F. Annanouch, E. Llobet, X. Correig, P. De Marco, C. Bittencourt, C. Blackman, Adv. Funct. Mater. 23 (2013) 1313–1322.
[16] G. He, M. Qiao, W. Li, Y. Lu, T. Zhao, R. Zou, B. Li, J.A. Darr, J. Hu, M.-M. Titirici, I.P. Parkin, Adv. Sci. 4 (2016) 1600214.
[17] Y.G. Shen, Y.W. Mai, Surf. Coat. Technol. 127 (2000) 239–246.
[18] S. Cong, Y. Tian, Q. Li, Z. Zhao, F. Geng, Adv. Mater. 26 (2014) 4260–4267.
[19] R. Zou, K. Xu, T. Wang, G. He, Q. Liu, X. Liu, Z. Zhang, J. Hu, J. Mater. Chem. A 1 (2013) 8560–8566.
[20] R. Zou, Z. Zhang, Q. Tian, G. Ma, G. Song, Z. Chen, J. Hu, Small 7 (2011) 3377–3384.
[21] Q. Liu, R. Zou, Y. Bando, D. Golberg, J. Hu, Prog. Mater. Sci. 70 (2015) 1–49.
[22] G. Kresse, J. Furthemüller, Comput. Mat. Sci. 6 (1996) 15–50.
[23] P.E. Blochl, Phys. Rev. B 50 (1994) 17953–17979.
[24] J.P. Perdew, K. Burke, M. Ernzerhof, Phys. Rev. Lett. 77 (1996) 3865–3868.
[25] J.P. Perdew, K. Burke, M. Ernzerhof, Phys. Rev. Lett. 78 (1997) 1396.
[26] H. J. Goldschmidt, Interstitial Alloy(London: Butterworths) (1967) 225.
[27] A.Y. Liu, R.M. Wentzcovitch, M.L. Cohen, Phys. Rev. B 38 (1988) 9483–9489.
[28] D.V. Suetin, I.R. Shein, A.L. Ivanovskii, Phys. Stat. Sol. B 245 (2008) 1590–1597.
[29] M. Kavitha, G. Sudha Priyanga, R. Rajeswarapalanichamy, K. Lykutti, J. Phys. Chem. Solids 77 (2015) 38–49.
[30] E.I. Isaev, S.I. Simak, I.A. Abrikosov, R. Ahuja, Yu Kh. Vekilov, M.I. Katsnelson, A.I. Lichtenstein, B. Johansson, J. Appl. Phys. 101 (2016) 123519.
[31] K. Balasubramanian, S. Khare, D. Gall, Phys. Rev. B 94 (2016) 174111.
[32] D.V. Suetin, I.R. Shein, A.L. Ivanovskii, J. Struct. Chem. 51 (2010) 199–203.
[33] M.J. Mehl, D. Finkenstadt, C. Dane, G.L.W. Hart, S. Curtarolo, Phys. Rev. B 91 (2015) 184110.
[34] L. Zhou, F.F. Klimashin, D. Holec, P.H. Mayrhofer, Scr. Mater. 123 (2016) 34–37.
[35] S.A. Shevlin, Z.X. Guo, J. Phys. Chem. C 112 (2008) 17456–17464.
[36] G. Henkelman, H. Jónsson, J. Chem. Phys. 113 (2000) 9978–9985.